

estimator is proven to be the MLE under the constraint that  $f_1$  and  $f_2$  are integer multiple of the step frequency  $f_s/N$ . Nevertheless, the MLE is in practice more appealing than the unwrapped FFT estimator since there is no need to calibrate the stimulus frequencies for achieving the optimality. Experiments have been carried out to corroborate the theoretical results.

## REFERENCES

- [1] M. L. Whitehead, B. B. Stagner, B. L. Lonsbury-Martin, and G. K. Martin, "Measurement of otoacoustic emissions for hearing assessment," *IEEE Eng. Med. Biol. Mag.*, vol. 13, pp. 210–226, 1994.
- [2] R. Probst, B. L. Lonsbury, and G. K. Martin, "A review of otoacoustic emissions," *J. Acoust. Soc. Amer.*, vol. 89, pp. 2027–2067, 1991.
- [3] A. N. Rasmussen and P. A. Osterhammel, "A new approach for recording distortion product oto-acoustic emissions," *Scand. Audiol.*, vol. 21, pp. 219–224, 1992.
- [4] F. J. Harris, "On the use of windows for harmonic analysis with the discrete Fourier transform," *Proc. IEEE*, vol. 66, pp. 51–83, Jan. 1978.
- [5] S. M. Kay, *Fundamentals of Statistical Signal Processing: Estimation Theory*. Englewood Cliffs, NJ: PTR Prentice-Hall, 1993.
- [6] R. S. Kulik and H. Kunov, "Results of two types of averaging for distortion product otoacoustic emission measurement," in *Proc. 17th IEEE EMBS Int. Conf.*, 1995, vol. 2, pp. 979–980.
- [7] S. M. Kay and V. Nagesha, "Maximum-likelihood estimation of signals in autoregressive noise," *IEEE Trans. Signal Processing*, vol. 42, pp. 88–101, Jan. 1994.
- [8] M. L. Whitehead, B. L. Lonsbury-Martin, and G. K. Martin, "The influence of noise on the measured amplitudes of distortion-product otoacoustic emissions," *J. Speech Hearing Res.*, vol. 36, pp. 1097–1102, 1993.
- [9] E. K. L. Hung and R. W. Herring, "Simulation experiments to compare the signal detection properties of DFT and MEM spectra," *IEEE Trans. Acoust., Speech, and Signal Processing*, vol. ASSP-29, pp. 1084–1090, May 1981.

## Estimating Cortical Potentials from Scalp EEG's in a Realistically Shaped Inhomogeneous Head Model by Means of the Boundary Element Method

Bin He,\* Yunhua Wang, and Dongsheng Wu

**Abstract**—Cortical potentials are estimated from scalp potentials using a realistically shaped inhomogeneous head model, by means of the boundary element method (BEM). A new adaptive algorithm has been developed to achieve high accuracy to link directly the cortical potentials to the scalp potentials in a realistically shaped inhomogeneous head model including the thin low-conductivity skull layer. Computer simulations using a concentric three-spheres head model have tested this approach. The present study demonstrates that the cortical potentials can be directly estimated from the scalp potentials using the BEM in a realistically shaped inhomogeneous head model.

**Index Terms**—Boundary element method (BEM), cortical imaging, electroencephalogram (EEG), head model, inverse problem.

## I. INTRODUCTION

Brain activation is a spatio-temporally-distributed process. While the electroencephalogram (EEG) offers excellent temporal resolution to characterize rapidly changing patterns of brain activation, conventional EEG techniques are limited mainly due to their limited ability to provide spatial information regarding brain activity. It is extremely desirable to image spatially distributed brain electrical activity from noninvasive electromagnetic recordings. Such noninvasive means would greatly increase our ability to accurately localize rapidly changing regional patterns of brain activation, and to aid presurgical evaluation in medically refractory epilepsy.

A number of investigators have attempted to improve the spatial resolution of the conventional EEG by solving the EEG inverse problem using equivalent dipole models or spatial enhancement approaches. Among many EEG inverse solutions, the spatial enhancement approaches [1]–[16] offer improved spatial resolution as compared to the conventional scalp EEG, meanwhile no *ad hoc* assumption is made on the underlying brain electrical sources. The unique feature of the spatial enhancement approach is its applicability to all kinds of brain electrical sources, thus, having the potential of achieving our ultimate goal of *imaging* brain electric activity.

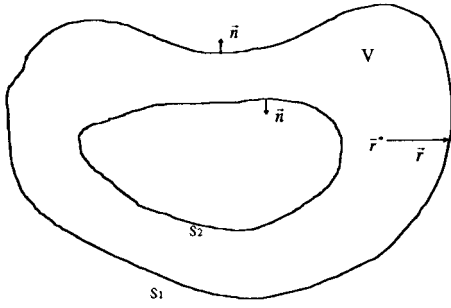
Of particular interest is the recent development of cortical potential (CP) imaging approaches, in which an explicit biophysical model of the passive conducting properties of a head is used to deconvolve a measured scalp potential (SP) distribution into a distribution of electrical potential on the cortical surface. Because the CP distribution can be experimentally measured [7], [17] and compared to the inverse imaging results, the CP imaging approach provides a powerful imaging means, which is also of physiologic importance. Furthermore, the CP's offer a much-enhanced spatial resolution in assessing the underlying brain activity as compared to the smeared SP's.

Manuscript received January 19, 1999; revised June 17, 1999. This work was supported in part by a grant from the Whitaker Foundation and by the National Science Foundation (NSF) under NSF CAREER Award BES-9875344. Asterisk indicates corresponding author.

\*B. He is with the Department of Electrical Engineering and Computer Science and the Department of Bioengineering, University of Illinois, 851 S. Morgan Street, Chicago, IL 60607 USA (e-mail: bhe@uic.edu).

Y. Wang and D. Wu are with the Department of Electrical Engineering and Computer Science, University of Illinois, Chicago, IL 60607 USA.

Publisher Item Identifier S 0018-9294(99)07420-0.


 Fig. 1. Volume  $V$  surrounded by surface  $S$ .  $S = S_1 \cup S_2$ .

## II. METHODS

### A. Cortical Imaging as a Linear Inverse Problem

The inverse problem has in general no unique solution, as the potential distribution measured on the outer surface of a volume conductor (VC) can be produced by an infinite number of sources within the VC [18]. However, when the inverse imaging problem is reduced to estimate the CP's from the SP's, the problem is unique, albeit ill-posed. The mathematical model linking an equivalent source generator and SP's can be represented as

$$\Phi = TX \quad (1)$$

where  $\Phi$  is the vector consisting of SP's,  $X$  is the unknown vector, which can be the equivalent source generator's parameters or the CP's, and  $T$  is the transfer matrix (TM).

There are two problems to be resolved in order to solve the CP inverse problem: a) to accurately construct the TM from the CP  $X$  to the SP  $\Phi$  and b) to inversely seek  $X$  from  $\Phi$ .

### B. Transfer Matrix in a Realistically Shaped Three-Shell Inhomogeneous Head Model

Green's second identity can be written as follows:

$$\iiint_V (A\nabla^2 B - B\nabla^2 A) dV = \iint_S (A\nabla B - B\nabla A) \cdot \vec{n} dS \quad (2)$$

where  $V$  is the volume inside the surface  $S$  and  $\vec{n}$  is the unit vector of the outward normal to the surface element (SE)  $dS$  as shown in Fig. 1.  $A$  and  $B$  are two scalar functions of position with continuous second derivatives within  $V$ .

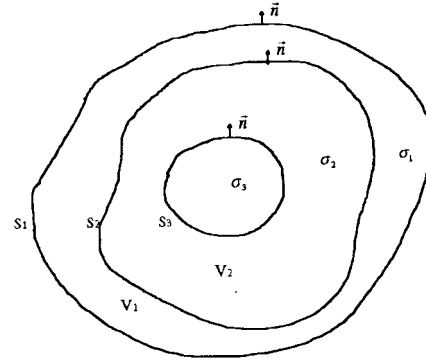
If  $V$  is an isotropic homogeneous VC and there is no current source existing within  $V$ , a useful result can be obtained by defining  $A$  as the scalar electrical potential  $u$  and  $B$  as  $1/r$ .  $r$  is the distance from the observation point  $\vec{r}^*$  located within  $V$  to the SE. In such case, the following equation can be obtained [19]:

$$u(\vec{r}^*) = \frac{1}{4\pi} \iint_S u \cdot d\Omega + \frac{1}{4\pi} \iint_S \frac{1}{r} \cdot \frac{\partial u}{\partial r_n} dS \quad (3)$$

where

- $u(\vec{r}^*)$  the electrical potential at the observation point  $\vec{r}^*$ ;
- $d\Omega$  the solid angle of an infinitesimal SE  $dS$  as seen from  $\vec{r}^*$ ;
- $\partial u / \partial r_n$  the first derivative of potential  $u$  with respect to the outward normal to  $dS$ .

Assume the head can be approximated by a three-shell VC as shown in Fig. 2, with the three shells representing the scalp, the skull, and the brain tissue, respectively. Assume each shell is homogeneous and each different shell has a different conductivity. Since brain electrical sources exist only inside the brain, there are no active


 Fig. 2. A three-shell volume conductor model. The volume between  $S_1$  and  $S_2$  is denoted as  $V_1$ , and that between  $S_2$  and  $S_3$  is denoted as  $V_2$ .

sources existing in the volume  $V_1$  and  $V_2$ . So Green's second identity can be applied to  $V_1$  and  $V_2$  separately. Applying (3) to the volume  $V_1$  results in

$$u(\vec{r}^*) = \frac{1}{4\pi} \iint_{S_1} u \cdot d\Omega - \frac{1}{4\pi} \iint_{S_2} u \cdot d\Omega - \frac{1}{4\pi} \iint_{S_2} \frac{1}{r} \cdot \frac{\partial u}{\partial r_n} dS. \quad (4)$$

By discretizing the surfaces  $S_1$  and  $S_2$  into triangle elements (TE's) and taking the limit of  $\vec{r}^*$  approaching the SE on  $S_1$  just from the inside of  $V_1$ , (4) becomes [19]

$$u_1^i = \frac{1}{4\pi} \sum_{j=1}^{N_1} u_1^j \Omega_1^{ij} - \frac{1}{4\pi} \sum_{j=1}^{N_2} u_2^j \Omega_2^{ij} - \frac{1}{4\pi} \sum_{j=1}^{N_2} \left( \frac{\partial u}{\partial r_n} \right)_2^j g_{12}^{ij} \quad (i = 1, \dots, N_1) \quad (5)$$

where

- $u_k^i$  the potential value at the  $i$ th TE on  $S_k$ ;
- $\Omega_k^{ij}$  the solid angle subtended by the  $j$ th triangle on  $S_k$  as seen from the  $i$ th TE on  $S_1$ . And  $\Omega_1^{ii} = 2\pi$ ;
- $N_k$  the number of discretized TE's on  $S_k$ ;
- $g_{12}^{ij} = \iint_{\Delta_j} dS / r_{ij}$  where  $\Delta_j$  is the  $j$ th TE on  $S_2$ , and  $r_{ij}$  is the distance between the  $i$ th TE on  $S_1$  and the  $j$ th TE on  $S_2$ .

Combining the left-hand side of (5) with the first term in the right-hand side of (5), and rewriting in matrix format, we get

$$P_{11}U_1 + P_{12}U_2 + G_{12}\Gamma_2 = 0 \quad (6)$$

where  $U_k$  is the column vector consisting of potentials at every SE on  $S_k$  and  $\Gamma_k$  is the column vector consisting of  $\partial u / \partial r_n$  at every TE on  $S_k$  but just inside of  $V_1$ .  $P_{11}$ ,  $P_{12}$ , and  $G_{12}$  are coefficient matrices with dimensions of  $N_1$  by  $N_1$ ,  $N_1$  by  $N_2$ , and  $N_1$  by  $N_2$ , respectively.

Similarly, take the limit of observation point  $\vec{r}^*$  approaching the SE on  $S_2$  just from the inside of  $V_1$ , we can get

$$P_{21}U_1 + P_{22}U_2 + G_{22}\Gamma_2 = 0. \quad (7)$$

Applying Green's second identity to the volume  $V_2$  between  $S_2$  and  $S_3$  produces two additional equations

$$P'_{22}U'_2 + P_{23}U_3 - G_{22}\Gamma'_2 + G_{23}\Gamma_3 = 0 \quad (8)$$

$$P_{32}U'_2 + P_{33}U_3 + G_{32}\Gamma'_2 + G_{33}\Gamma_3 = 0 \quad (9)$$

where  $U'_2$  is the column vector consisting of potentials at every SE on  $S_2$  and  $\Gamma'_2$  is the column vector consisting of  $\partial u / \partial r_n$  at every

TE on  $S_2$  but just inside of  $V_2$ . The boundary conditions on  $S_2$  can be expressed as follows:

$$U'_2 = U_2, \sigma_1 \Gamma_2 = \sigma_2 \Gamma'_2. \quad (10)$$

Solving (6) and (7) leads to

$$U_2 = (G_{12}G_{22}^{-1}P_{22} - P_{12})^{-1}(P_{11} - G_{12}G_{22}^{-1}P_{21})U_1 = T_{21}U_1 \quad (11)$$

$$\Gamma_2 = -G_{22}^{-1}(P_{21} + P_{22}T_{21})U_1 \quad (12)$$

where  $T_{21} = (G_{12}G_{22}^{-1}P_{22} - P_{12})^{-1}(P_{11} - G_{12}G_{22}^{-1}P_{21})$ . From (8)–(12), the following equation can be derived:

$$\left[ \begin{aligned} &(P'_{22} - G_{23}G_{33}^{-1}P_{32})T_{21} + \frac{\sigma_1}{\sigma_2}(I + G_{23}G_{33}^{-1}G_{32}G_{22}^{-1}) \\ &\cdot (P_{21} + P_{22}T_{21}) \end{aligned} \right] U_1 = (G_{23}G_{33}^{-1}P_{33} - P_{23})U_3. \quad (13)$$

Denote  $A = (P'_{22} - G_{23}G_{33}^{-1}P_{32})T_{21} + (\sigma_1/\sigma_2)(I + G_{23}G_{33}^{-1}G_{32}G_{22}^{-1})(P_{21} + P_{22}T_{21})$

$$B = G_{23}G_{33}^{-1}P_{33} - P_{23}.$$

Equation (13) can be rewritten as

$$AU_1 = BU_3.$$

So, the CP  $U_3$  can be related to the SP  $U_1$  by

$$U_1 = T_{13}U_3 \quad (14)$$

where  $T_{13} = A^\#B$ , and  $A^\#$  is the pseudoinverse of the matrix  $A$ . The matrix  $T_{13}$  is the TM from the CP's to the SP's, and is the same as the matrix  $T$  in (1).

The calculation of coefficients  $g_{kl}^{ij} = \iint_{\Delta_j} dS/r_{ij}$  ( $i = 1 \cdots N_k$ ,  $j = 1 \cdots N_l$ ) contributes to a significant degree the numerical accuracy of the TM. Due to the proximity of each layer and the significant change in conductivity, an adaptive approach has been developed to achieve high accuracy in the TM. Let each shell of the head model consist of  $N_1$ ,  $N_2$ , and  $N_3$  TE's, respectively. Each TE was further divided into  $L$  subelements in calculating the coefficients  $g_{kl}^{ij}$ . Fig. 3 illustrates this numerical strategy when  $L = 4$ , while a number larger than four is used in the present study. The number of subtriangles  $L$  is determined when the following inequality is satisfied:

$$\left| \frac{g_{kl}^{ij}[n] - g_{kl}^{ij}[n-1]}{g_{kl}^{ij}[n]} \right| \leq \varepsilon$$

where  $\varepsilon$  is a small positive number adjusting the accuracy desired, and  $g_{kl}^{ij}[n]$  refers to the value of the coefficient  $g_{kl}^{ij}$  at the  $n$ th iteration. For each triangle, the averaged value over the subtriangles is used as the element in the coefficient matrix for  $\gamma_k$  where  $\gamma_k$  refers to the first derivative of the potential on the  $k$ th surface.

To calculate the elements of matrices  $P$ 's, the analytic expression in reference [20] was adopted in the present study to get the solid angle subtended by a TE as seen from an observation point.

In practice, the vector of the measured SP's  $\Phi$  is a subset of the potential vector  $U_1$  in (14). Therefore, the SP measurements can be connected with the CP's by the submatrix of  $T_{13}$ ,  $T$

$$\Phi = TU_3 \quad (15)$$

where  $T$  is the  $N$  by  $N_3$  coefficient matrix with the rows being a subset of the rows in  $T_{13}$ .  $N$  is the number of the scalp electrodes, and  $N_3$  is the number of the discretized TE's on the brain surface. Notice that  $T$  is determined only by the model geometry and the ratio between the conductivity of the scalp and the skull.

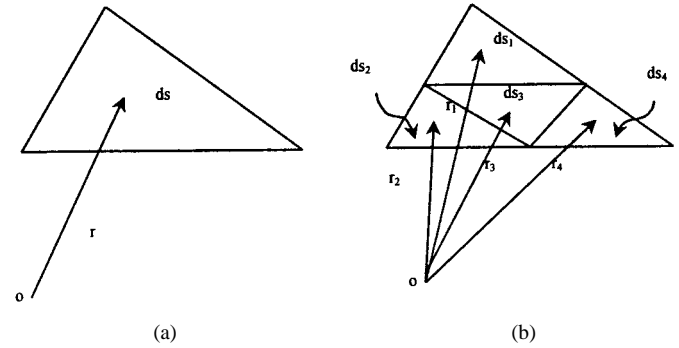


Fig. 3. Illustration of the adaptive numerical algorithm developed in the present study. (a) Previous method:  $ds/r$  is used as the integral element. (b) Present method:  $ds/r$  is replaced by  $\sum_{i=1}^L (ds_i/r_i)$ . The number of the subtriangles is assumed to be four in this illustration.

### C. Regularization Strategy for Inversion of the Transfer Matrix

As the measurement electrode number is always much smaller than the dimension of the unknown vector  $X$ , and measurement noise always exists, the EEG CP imaging inverse problem is an ill-posed, underdetermined problem.

Since there is always noise existing in scalp measurements, (1) should be modified to

$$\Phi = TX + n \quad (16)$$

where  $n$  is a noise vector whose dimension is the same as the scalp recording data. Based on (16), a least-square estimate can be obtained by minimizing the following objective function:

$$O(X) = \|\Phi - TX\|^2 \rightarrow \min. \quad (17)$$

For an arbitrary matrix, we have [21]

$$X = (T^t T)^+ T^t \Phi = T^t (T T^t)^+ \Phi = T^+ \Phi \quad (18)$$

where  $()^+$  signifies the *general inverse*. The general inverse solution is a minimum norm (MN) solution among the infinite set of solutions which satisfy the scalp measurement potentials.

The singular value decomposition (SVD) procedure [2]–[4] can be used to obtain the general inverse in (18). The effects of noise can be reduced by using the method of the truncated SVD method. The determination of the truncation level in the SVD procedure can be made based on the discrepancy principle [22], in which the truncation level is determined such that the following equation is satisfied:

$$\|TX - \Phi\| = \|n\| \quad (19)$$

where  $\|n\|$  is the noise level in the measurements.

As a result, the CP estimate can be represented by

$$\hat{U}_3 = \hat{X} = T^\# \Phi \quad (20)$$

where,  $\hat{U}_3$  is the estimated CP field (that is, the unknown vector  $X$  in the above discussion).

## III. RESULTS

Computer simulations were conducted to test the present BEM-based CP imaging algorithms. A concentric three-shell sphere head model [23] was employed because of the availability of the analytic solution of potential fields. In the three-shell sphere model, the values of radii were taken as 1.0, 0.92, and 0.87, respectively. The value of conductivity ratio is taken as 1/80. Each surface of the three-shell sphere was discretized uniformly into 1280 TE's. The forward matrix  $T_{13}$  was calculated according to (5)–(14).

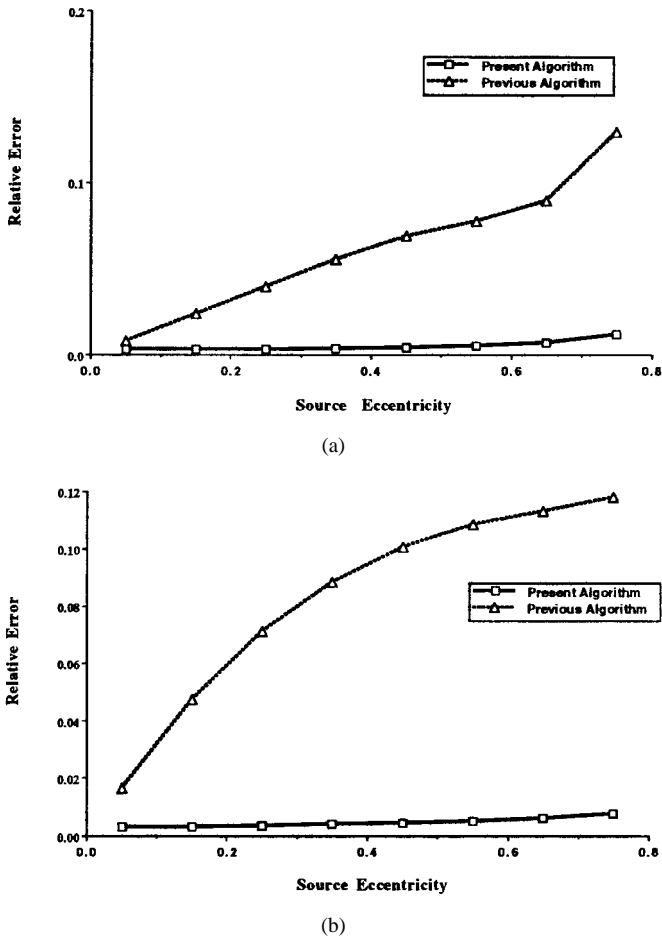


Fig. 4. The accuracy of the numerical forward solution. The horizontal axis refers to the eccentricity of the dipole sources and the vertical axis refers to the relative error: (a) radial dipole sources and (b) tangential dipole sources. See text for details.

It is of importance to construct the TM with high accuracy from the CP's to the SP's, when the skull low-conductivity region is considered. The numerical accuracy of the present forward BEM algorithm was evaluated. Fig. 4 shows relative errors (RE's) of the numerical forward solutions (as compared with the analytical solutions) for the concentric three-shell sphere head model. The horizontal axis refers to the eccentricity of the dipole sources and the vertical axis refers to the RE between the TM-based numerical forward solution and the analytical SP generated directly by the two current dipole sources. The two dipole sources were located at  $(\pm r \cdot \sin(\pi/4), 0, r \cdot \cos(\pi/4))$  with varying eccentricity  $r$ . The dipoles were either oriented (both) radially [Fig. 4(a)] or (both) tangentially [Fig. 4(b)]. Rectangles and triangles refer to the results obtained by using the present numerical algorithm and obtained by applying Barr's algorithm [19] to the three-shell inhomogeneous head model. Fig. 4 clearly demonstrates that the present BEM algorithm can achieve high numerical accuracy in constructing the TM even if the low-conductivity skull inhomogeneity is considered. It is valuable to note that the adaptive numerical algorithm described in Section II-B plays an important role in achieving this numerical accuracy. Simple application of Barr's algorithm [19], which was developed for a homogeneous VC, to the three-shell inhomogeneous head model, does not lead to satisfactory numerical accuracy in computing the SP's from the CP's.

Different electrode configurations—640 electrodes, 310 electrodes, 128 electrodes, and 65 electrodes located uniformly over the upper

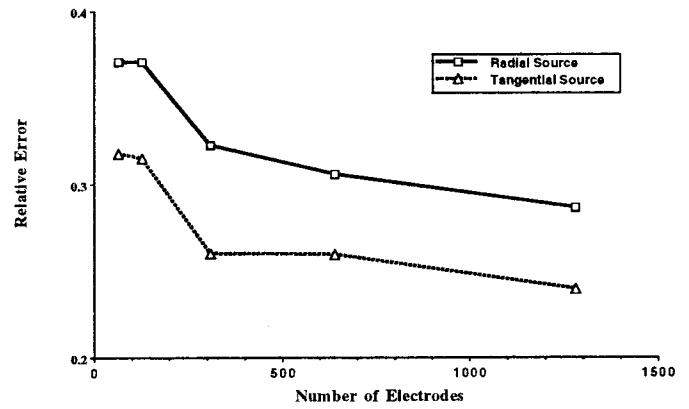


Fig. 5. Effect of scalp electrode numbers on the present cortical-potential imaging. The horizontal axis refers to the number of electrodes, and the vertical axis refers to the relative error. The results obtained by using all-sphere 1280 electrodes are also shown to serve as a reference. Different electrode configurations—640 electrodes, 310 electrodes, 128 electrodes, and 65 electrodes located uniformly over the upper hemisphere, were employed in the simulation, in which 10% GWN was added to the scalp potentials.

hemisphere, were employed in the simulation to test the present imaging algorithm. Fig. 5 shows the RE for different electrode systems compared to the all-sphere 1280 electrode system when 10% Gaussian white noise (GWN) was considered. (The noise level is defined as the ratio of the standard deviation of noise and the root of the power of the SP. Ten trials of GWN distributions were simulated and the results presented here are the averaged values over these trials.) The locations of the dipole sources are  $(\pm 0.65 \cdot \sin(\pi/4), 0, 0.65 \cdot \cos(\pi/4))$ . The horizontal axis refers to the number of electrodes, and the vertical axis refers to the RE. Rectangles and triangles refer to the radial and tangential dipoles, respectively. The dipoles were both radially or tangentially oriented. The RE's refer to the error between the estimated CP and the analytical CP. In this simulation, the subvector  $\Phi$  of the  $U_1$ , which consists of 640, 310, 128, or 65 (or 1280) potentials over the scalp, was used. Fig. 5 demonstrates the applicability of the present BEM-based CP imaging approach to a practical environment, in which the number of electrodes is limited.

#### IV. DISCUSSION

The present study demonstrates that one can *directly* estimate the CP's from the SP's in a realistically shaped inhomogeneous head model by means of the BEM. Barr's algorithm has previously been applied to relate the CP's with the SP's in a homogeneous head VC [6]. The inclusion of the significant low-conductivity inhomogeneity in the head model necessitates the development of the present adaptive numerical algorithm in order to achieve high precision in constructing the forward TM.

Theoretically, the potential field at the cortical surface is uniquely specified by the SP field. The electrical characteristics of the brain tissue have no role in this method. Compared to the fine work of BEM-based indirect method of estimating CP's [11], which is based on the isolated problem approach [24], there is no need in the present approach to model the electrically activated brain regions by current dipoles. The present approach is based only on the scalp EEG measurement, the geometry measurement and the conductivity ratio between the scalp and the skull. Previously, the finite element method has been elegantly applied to estimate the CP's from the SP's [5], [7]. However, use of the BEM represents significant cost reduction in computation, while concurrently accounting for the realistic geometry of the head and the significant inhomogeneity such as the skull. The

effect of the CSF could also be incorporated by applying the present numerical algorithm to a four-shell VC model.

The numerical algorithm developed in the present work provides a new means of linking the CP's with the SP's with high accuracy, when a thin low-conductivity skull layer exists. It is uniquely different from the well-known isolated program approach [24], which treats the numerical calculation of the SP's due to assumed dipole sources in the brain. The present adaptive algorithm improves substantially the numerical accuracy of the forward solution of the SP's from the CP's when a thin low-conductivity skull layer exists. Introduction of the use of linear interpolation of the potential over the SE's shall further improve the numerical accuracy of the forward TM linking the CP's and SP's.

The inversion of the transfer matrix has been achieved by applying the concept of the general inverse. Similar to other deconvolution methods, noise in the SP measurements is a main factor affecting the inverse results. Truncated SVD procedures are used to implement the noise-suppression functions. The discrepancy principle [22] is used to obtain a reasonable estimate of the CP's under realistic noise. The inversion of the TM can also be realized by considering the constrained inverse problem via regularization schemes.

In summary, the present BEM approach provides a highly accurate direct means to link the CP's and the SP's, taking both the head geometry and skull conductivity inhomogeneity into consideration. Due to the flexibility and efficiency of the BEM algorithm, the present approach provides a promising means to further our capability of estimating cortical potentials noninvasively.

#### ACKNOWLEDGMENT

The authors would like to thank D. Yao for useful discussions on the inverse regularization algorithms.

#### REFERENCES

- [1] W. Freeman, "Use of spatial deconvolution to compensate for distortion of EEG by volume conductor," *IEEE Trans. Biomed. Eng.*, vol. BME-27, pp. 421–429, Aug. 1980.
- [2] M. Hamalainen and R. Ilmoniemi, "Interpreting measured magnetic fields of the brain: Estimates of current distributions," Helsinki Univ., Helsinki, Finland, Tech. Rep. TKK-F-A559, 1984.
- [3] M. Sidman, G. Ford, Ramsey, and C. Schlichting, "Age-related features of the resting and P300 auditory evoked responses using the dipole localization method and cortical imaging technique," *J. Neurosci. Methods*, vol. 33, pp. 23–32, 1990.
- [4] J. Z. Wang, S. J. Williamson, and L. Kaufman, "Magnetic source images determined by a lead-field analysis: The unique minimum-norm least-squares estimation," *IEEE Trans. Biomed. Eng.*, vol. 39, pp. 665–675, July 1992.
- [5] J. Le and A. Gevins, "Method to reduce blur distortion from EEG's using a realistic head model," *IEEE Trans. Biomed. Eng.*, vol. 40, pp. 517–528, June 1993.
- [6] R. Srebro, R. M. Oguz, K. Hughlett, and P. D. Purdy, "Estimating regional brain activity from evoked potential field on the scalp," *IEEE Trans. Biomed. Eng.*, vol. 40, pp. 509–516, June 1993.
- [7] A. Gevins, J. Le, N. K. Martin, P. Brickett, J. Desmond, and B. Reutter, "High-resolution EEG: 124-channel recording, spatial deblurring and MRI integration methods," *Electroenceph. Clin. Neurophysiol.*, vol. 90, pp. 337–358, 1994.
- [8] P. Nunez, R. B. Silibertein, P. J. Cdush, R. S. Wijesinghe, A. F. Westdrop, and R. Srinivasan, "A theoretical and experimental study of high-resolution EEG based on surface Laplacian and cortical imaging," *Electroenceph. Clin. Neurophysiol.*, vol. 90, pp. 40–57, 1994.
- [9] B. He, Y. Wang, S. Pak, and Y. Ling, "Cortical source imaging from scalp electroencephalograms," *Med. Biol. Eng. Comput.*, vol. 34, pp. 257–258, 1996.
- [10] B. He, Y. Wang, and D. Wu, "Imaging brain electrical activity using a 3-D realistically shaped inhomogeneous head model," in *Proc. IEEE/EMBS*, 1997, pp. 1167–1169.
- [11] F. Babiloni, C. Babiloni, F. Carducci, L. Fattorini, C. Anello, P. Onorati, and A. Urbano, "High-resolution EEG: A new model-dependent spatial deblurring method using a realistically-shaped MR-constructed subject's head model," *Electroenceph. Clin. Neurophysiol.*, vol. 102, pp. 69–80, 1997.
- [12] F. Zanow, "Realistically shaped models of the head and their applications to EEG and MEG," Ph.D. dissertation, Univ. Twente, Twente, the Netherlands, 1997.
- [13] J. W. Phillips, R. M. Leahy, and J. C. Mosher, "MEG-based imaging of focal neuronal current sources," *IEEE Trans. Med. Imag.*, vol. 16, pp. 338–348, June 1997.
- [14] Y. Wang and B. He, "A computer simulation study of cortical imaging from scalp potentials," *IEEE Trans. Biomed. Eng.*, vol. 45, pp. 724–735, June 1998.
- [15] B. He, "High resolution source imaging of brain electrical activity," *IEEE Eng. Med. Biol.*, vol. 17, no. 5, pp. 123–129, 1998.
- [16] G. Edlinger, P. Wach, and G. Pfurtscheller, "On the realization of an analytic high-resolution EEG," *IEEE Trans. Biomed. Eng.*, vol. 45, pp. 736–745, June 1998.
- [17] V. L. Towle, S. Cohen, N. Alperin, K. Hoffmann, P. Cogen, J. Milton, R. Grzeszczuk, C. Pelizzari, I. Syed, and J. P. Spire, "Displaying electrocorticographic findings on gyral anatomy," *Electroenceph. Clin. Neurophysiol.*, vol. 94, pp. 221–228, 1995.
- [18] H. von Helmholtz, "Über einige gesetzeder verbeitung elektrischer strome in koperlichen leitern mit anwendung auf die theorischelektrischen versuche," *Ann. Physik. u. Chem.*, vol. 89, pp. 211–233; 353–377, 1853.
- [19] R. C. Barr, M. Ramsey, III, and M. S. Spach, "Relating epicardial to body surface potential distributions by means of transfer coefficients based on geometry measurements," *IEEE Trans. Biomed. Eng.*, vol. BME-24, pp. 1–11, Jan. 1977.
- [20] A. Van Oosterom and J. Strackee, "The solid angle of a plane triangle," *IEEE Trans. Biomed. Eng.*, vol. BME-30, pp. 125–126, Feb. 1983.
- [21] G. H. Golub and C. F. Van Loan, *Matrix Computations*, 2nd ed. Baltimore, MD: Johns Hopkins Univ. Press, 1989.
- [22] V. A. Morozov, *Methods for Solving Incorrectly Posed Problems*. Berlin, Germany: Springer-Verlag, 1984.
- [23] S. Rush and D. A. Driscoll, "EEG electrode sensitivity—An application of reciprocity," *IEEE Trans. Biomed. Eng.*, vol. BME-16, pp. 15–22, Jan. 1969.
- [24] M. S. Hamalainen and J. Sarvas, "Realistic conductor geometry model of the human head for interpretation of neuromagnetic data," *IEEE Trans. Biomed. Eng.*, vol. 36, pp. 165–171, Feb. 1989.